Vol. 92 No. 5 pp. 1901–1916 ACTA GEOLOGICA SINICA (English Edition) Oct. 2018

Evolution of Tectonic Uplift, Hydrocarbon Migration, and Uranium Mineralization in the NW Junggar Basin: An Apatite Fission-Track Thermochronology Study

QIN Mingkuan[1, 2], HUANG Shaohua[1, 2, *], HE Zhongbo[1, 2], XU Qiang[1, 2], SONG Jiye[1, 2], LIU Zhangyue[1, 2] and GUO Qiang[1, 2]

1 *Beijing Research Institute of Uranium Geology, Beijing 100029, China*

2 *CNNC Key Laboratory of Uranium Resources Exploration and Evaluation Technology, Beijing 100029, China*

Abstract: The Mesozoic–Cenozoic tectonic movement largely controls the northwest region of the Junggar Basin (NWJB), which is a significant area for the exploration of petroleum and sandstone-type uranium deposits in China. This work collected six samples from this sedimentary basin and surrounding mountains to conduct apatite fission track (AFT) dating, and utilized the dating results for thermochronological modeling to reconstruct the uplift history of the NWJB and its response to hydrocarbon migration and uranium mineralization. The results indicate that a single continuous uplift event has occurred since the Early Cretaceous, showing spatiotemporal variation in the uplift and exhumation patterns throughout the NWJB. Uplift and exhumation initiated in the northwest and then proceeded to the southeast, suggesting that the fault system induced a post spread-thrust nappe into the basin during the Late Yanshanian. Modeling results indicate that the NWJB mountains have undergone three distinct stages of rapid cooling: Early Cretaceous (ca. 140–115 Ma), Late Cretaceous (ca. 80–60 Ma), and Miocene–present (since ca. 20 Ma). These three stages regionally correspond to the Lhasa-Eurasian collision during the Late Jurassic–Early Cretaceous (ca. 140–125 Ma), the Lhasa-Gandise collision during the Late Cretaceous (ca. 80–70 Ma), and a remote response to the India-Asian collision since ca. 55 Ma, respectively. These tectonic events also resulted in several regional unconformities between the J_3/K_1, K_2/E, and E/N, and three large-scale hydrocarbon injection events in the Piedmont Thrust Belt (PTB). Particularly, the hydrocarbon charge event during the Early Cretaceous resulted in the initial inundation and protection of paleo-uranium ore bodies that were formed during the Middle–Late Jurassic. The uplift and denudation of the PTB was extremely slow from 40 Ma onward due to a slight influence from the Himalayan orogeny. However, the uplift of the PTB was faster after the Miocene, which led to re-uplift and exposure at the surface during the Quaternary, resulting in its oxidation and the formation of small uranium ore bodies.

Key words: apatite fission track, tectonic uplift, hydrocarbon migration, sandstone-type uranium deposit, NW Junggar Basin

1 Introduction

The evolution of the NW Junggar Basin, located in the northwestern part of China, is related to the interactions between the Kazakhstan Plate and the Junggar Massif boundary (Sui Fenggui, 2015). Paleozoic rifting and oceanic spreading were followed by convergence, subduction, and collision that occurred from the Late Carboniferous onwards, resulting in complex present-day geological structures (Fig. 1) (Zhao Bai, 1992; Allen et al., 1997; Wang Renfu, 2011). The study area is located in the western region of the NNE-trending Junggar orogenic belt (WJOB), which comprises the Piedmont Thrust Belt (PTB) that stretches ca. 250 km from the SW to the NE (Fig. 1c). The Zaire and Halaalate Mountains, located in the WJOB, are the source area for sedimentary infill in the PTB (Song Jiye et al., 2015). The PTB is rich in oil and

* Corresponding author. E-mail: huangshaohua20@126.com

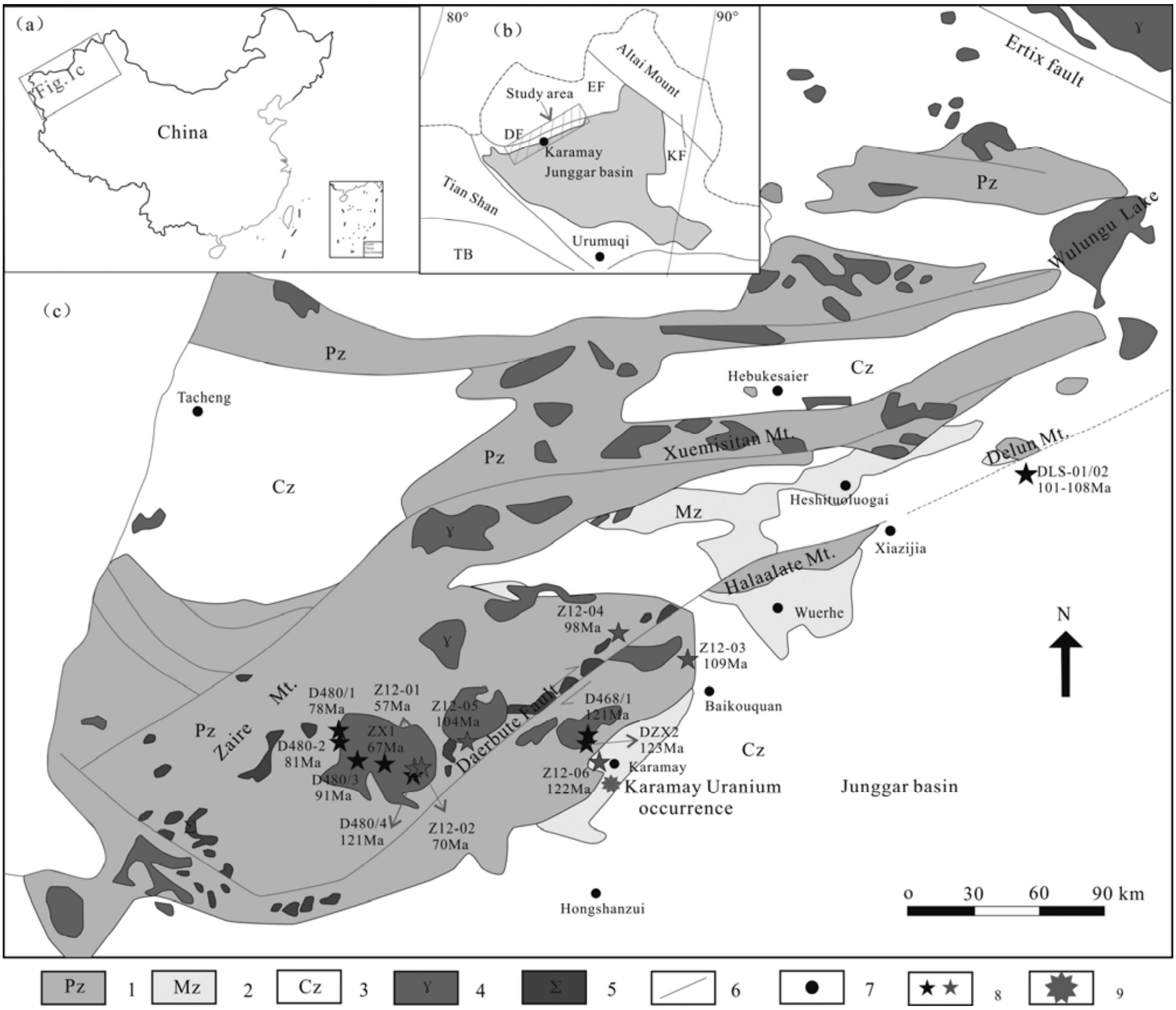

Fig. 1. Simplified geological map of the NW Junggar Basin and surrounding regions with apatite fission-track ages (China basemap after China National Bureau of Surveying and Mapping Geographical Information; Li Wei, 2007; Chen et al., 2011).
1, Paleozoic; 2, Mesozoic; 3, Cenozoic; 4, granite; 5, ophiolite; 6, fault; 7, place; 8, sampling location; 9, Uranium occurrence.

gas resources, such as the Karamay oilfield, which is the largest oilfield in NW China, and the Hongshanzui, Heiyoushan, and Baijiantan oil-sand ore deposits (Fig. 2), which are globally famous oil-sand ore fields (Chen Jianping, 2002; Zhang Shanwen, 2013). In the Karamay area, drilling teams (the No. 519 Geological Team in 1950s and the No. 216 Geological Team in 2002) discovered several uranium occurrences (Fig. 1) (Lu Kegai, 2005). Based on these drilling investigations, a new metallogenic hypothesis for the formation of the interlayered, oxidation, sandstone uranium deposits emerged which suggests that the PTB is potentially a significant region for the exploitation of sandstone uranium deposits. The PTB, therefore, is an excellent field area for studying the relationship between hydrocarbon deposits and uranium mineralization.

Tectonic evolution is a key factor that controls the distribution of oil and gas and the location of uranium deposits in the basin (He Zhongbo et al., 2014; Sui Fenggui, 2015). As one of the most important and well-established thermochronologic approaches, AFT thermochronology can be used to reveal the tectonic uplift history within the upper 2–4 km of crust over geological time scales (Yuan Wanming et al., 2007), and has been applied to constrain a range of geological processes (Du Zhili et al., 2007; Silvia et al., 2014; Paulo et al., 2015; Eva et al., 2016). The Junggar Basin was formed in a compressional structural environment, exhibiting the basic characteristics of multi-stage tectonic evolution and a composite superposition system (Ma Delong, 2014; Yang Yongqiang et al., 2017). Recently, several AFT thermochronology studies of the NWJB have found

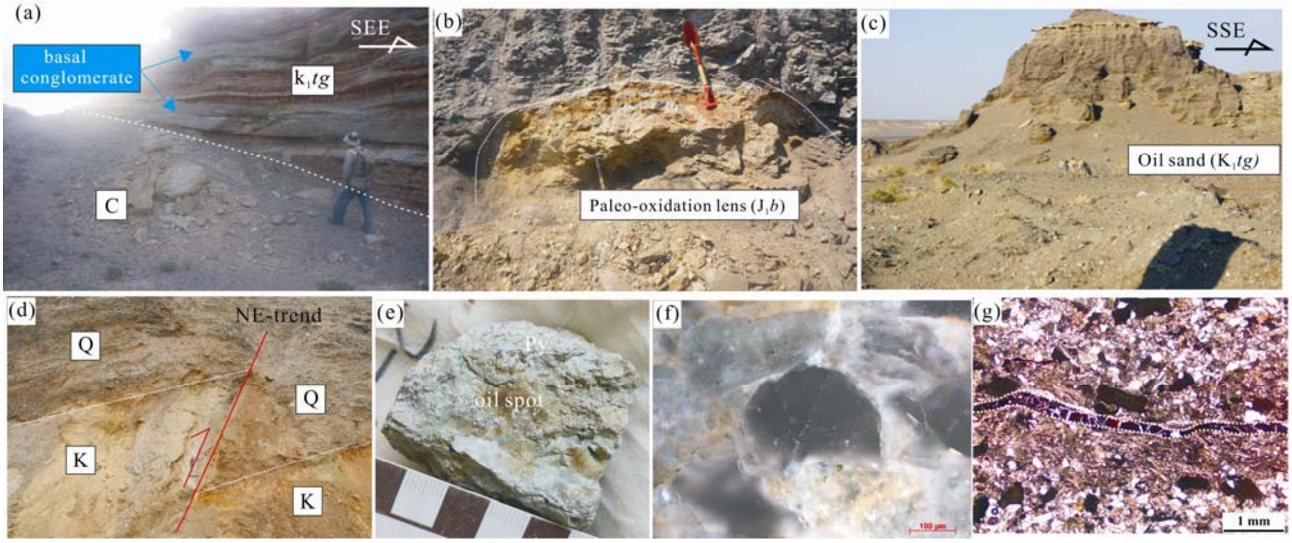

Fig. 2. Field geological photographs in the NW Junggar Basin.
(a), Cretaceous overlay above Carboniferous strata; (b), black oil sands with wrapped yellow oxidizing lens; (c), lower Cretaceous oil sands; (d), quaternary fault structure; (e), subsequent granular pyrite associated with black oil patch in the altered greenish sandstone; (f), light oil added to micro-fractures showing light blue fluorescence; (g), black bitumen veins (light).

evidence for the occurrence of two rapid exhumation events during the periods of approximately 145–90 Ma and 29–9 Ma (Li Wei, 2007; Li Li et al., 2008). Also, several other studies have attempted to understand the correlations between tectonic activity and hydrocarbon accumulation/dissipation (He Dengfa et al., 2004; Xu Jiandong et al., 2008; Tan Kaijun et al., 2008; Sui Fenggui, 2015), tectonic evolution, and uranium mineralization (Lin Shuangxing, 1997; Chen Zhengle et al., 2006, 2011; He Zhongbo et al., 2014). In addition, the impact of hydrocarbon migration and groundwater movement on uranium mineralization was studied using hydrochemistry and stable isotopic techniques (Feng Shirong, 1998; Zhang Quanqing et al., 2009). Although several studies on uranium metallogenic conditions, characteristics, and models of the study area exist (Lu Kegai, 2005), the relationships between hydrocarbon migration, uranium mineralization, and ore-forming processes remain unknown.

The aim of this study is to reconstruct the tectono-thermal evolution of the NWJB by using a new AFT dataset built from analyses of metamorphic, sedimentary, and intrusive rocks sampled from the Zaier Mountains and the PTB, in combination with existing low-temperature thermochronological data (Li Wei, 2007; Li Li et al., 2008). Based on our field investigations, stratigraphic correlations, and hydrocarbon accumulation and U-mineralization characteristics, we use the results of apatite fission track to discuss various aspects of hydrocarbon migration and uranium mineralization during the Mesozoic and Cenozoic.

2 Geological Setting

2.1 Regional geological evolution

The northwestern margin of the Junggar Basin has experienced four tectonic movements since the Late Paleozoic, i.e., the Hercynian, Indosinian, Yanshan, and Himalayan (Franco et al., 2011; Hu Yang et al., 2012; Muhammad et al., 2016). These movements correspond to multiple strata unconformities in the PTB: P_1j/C, P_1f/P_1j, T/P_2w, J_1b/T, J_1b/J_1s, J_2x/J_1s, and K/J (Figs. 2a and 3) (Ma Delong, 2014). During the late stages of the Early Paleozoic, a number of minor blocks and accretionary terranes drifting throughout the Paleo-Asian Ocean collided and merged together to form the Kazakhstan Paleo-plate, which was located adjacent to the Tarim Plate’s northern coast and the Siberian Plate’s southern coast (Du Shekuan, 2004; Huang Shaohua et al, 2016; Liu Zhangyue et al., 2015). The NWJB is situated along the eastern edge of the Kazakhstan Paleo-plate (Fig. 1). The WJOB is characterized by extensive island-arc volcanics, granitic intrusives, Paleozoic ophiolitic mélanges (Franco et al., 2011; Yang Yongqiang et al., 2017), and marine sediments, which are the main sources of uranium-bearing clastics in the PTB (Song Jiye et al., 2015). Many studies have demonstrated that the end of the late Carboniferous was an important turning point for the evolution of the Junggar Basin (Allen et al., 1997; Chang et al., 2012; Sui Fenggui, 2015; Qi et al., 2016). The Kazakhastan Plate extruded eastward, and the West Junggar Oceanic Crust subducted into the Kazakhstan plate, followed by intercontinental collision after oceanic basin closure and the formation of the West Junggar Landmass (He Dengfa et al., 2004; Ma Delong, 2014). Then, this area entered into a post-collisional orogenic period involving four evolutionary stages (Hu Yang et al., 2012), i.e., the Permian (P), Triassic (T), Jurassic–Cretaceous (J–K), and Cenozoic (C).

The most intense tectonic activity occurred during the Permian (Sui Fenggui, 2015). During the Early Permian, the NWJB was in a post-orogenic extensional setting (Wu Yuanyan et al., 2002; Xu Jiandong et al., 2008; Zhang Shanwen, 2013). Delamination of subducted plates caused thinning and stretching of the regional lithosphere, which induced large-scale tectono-magmatic events associated with the post collision extension (290±Ma) that formed numerous Early Permian granite intrusions, basalts, and rhyolitic volcanic rocks (Ma Delong, 2014). Meanwhile, the present-day shape of the piedmont foreland basin began to form, where the sedimentary strata tended to wedge inward and become thinner from the basin margin (Du Shekuan, 2004; Wang Renfu, 2011). At the end of Permian, with the presence of continuous NW-SE extrusion of the Kazakhstan plate toward the Junggar block, the initiation of the Indosinian Movement led to more intense nappe and extrusion events, which resulted in the development of troughs along the Junggar Basin margin that fold into mountains and formed the collisional -type Junggar foreland basin (He Dengfa et al., 2004, 2007). During the Triassic, the NWJB retained its previous structural pattern. The late Permian stress field continued todominate, while tectonic intensity became marginally weaker (Sui Fenggui, 2015). High-angle thrusting that occurred in the Permian induced intense extrusion processes and further strengthened tectonic structures, resulting in the formation of the NWJB's eventual architecture in the late Triassic (Li Wei, 2007; Li Li et al., 2011). During this stage, the basin gradually changed from a foreland basin to an intracontinental depression basin, and entered an oscillation stage of recurring subsidence and uplift events (Ma Delong, 2014). The PTB deposited Triassic alluvial fan and fan delta strata, and this sedimentary center gradually migrated toward the interior of the basin (Yang Yongqiang et al., 2017). Nevertheless, the late Indosinian movement led to the denudation of sediment in the PTB, forming angular unconformities between the Jurassic and Triassic Formations (Sui Fenggui, 2015). During the Jurassic–Cretaceous, tectonic activity further weakened. Overlying strata gradually overlapped and buried the thrust belt which was basically inactive before (Stijin et al., 2016). The absence of faults and folds, and the presence of multi-episodic local unconformities which have constant thicknesses in the Jurassic–Cretaceous strata, record the preoscillation history of this basin (Tan Kaijun et al., 2008). Evidence of this oscillatory history comes from the Lower Jurassic Sangonghe Formation, which was deposited during a significant period of lake transgression. The Lhasa collision (140–125 Ma) resulted in a NW trending regional tectonic movement throughout the NWJB (Bai Guojuan, 2009), which induced strong Middle and Upper Jurassic Formation erosion in the PTB, leading to regional unconformable contact between the Jurassic and Cretaceous Formation (He Dengfa et al., 2007). Following this Jurassic erosion event, the early Cretaceous was a period of relaxation or calm as far as tectonic, magmatic, or erosional events are concerned (Zhang Shanwen, 2013). The entirety of the PTB subsided and received extensive overlying deposits (Fig. 2a). During the late Cretaceous, the study area experienced southward uplift, via multi-phase crustal uplift and subsidence (Zhao Bai, 1992; Zhang Quanqing et al., 2009), which resulted in slow west-trending uplift and regional erosion of the Cretaceous Formation.

During the Cenozoic, the well-known Indosinian-Eurasian Collision led to uplift in the North Tianshan Orogeny (Huang Shaohua et al., 2016; Muhammad et al., 2016; Liu Zhangyue et al., 2017). However, this did not influence or result in significant tectonic activity in the study area (Wu Yuanyan et al., 2002). Cenozoic products are commonly absent in the PTB (Lin Shuangxing, 1997), because the area was not significantly influenced by Himalayan orogenesis (Shao Yu et al., 2011).

2.2 Characteristics of hydrocarbon accumulation

The NWJB is characterized by multiple types of source rocks and stages of hydrocarbon generation, filling and accumulation events, and multiple-stage destruction (Chen Jianping et al., 2016). Hydrocarbon mainly originates from the Permian Fengcheng and Wuerhe source rocks (Fig. 3) located in the NE-oriented Mahu depression situated in the east of the study area (Chen Jianping, 2002; Bai Guojuan, 2009). Large amounts of oil were derived from the Fengcheng source rock during the late Triassic–Jurassic period, with a present day Ro of 1.34%, whereas the Wuerhe source rock generated oil during the Jurassic–Cretaceous (Chen Jianping et al., 2016). A Z-shaped migration network characterizes the migration pathways, which contain the Karamay–Xiazijie fault belt and its secondary faults, stratigraphic unconformities, and clastic rock with good porosity and permeability (Fig. 3) (Hu Yang et al., 2012; Shen Yang et al., 2015). Generally, the migration direction follows a step-type hydrocarbon accumulation model in the following steps (Wang Huimin et al., 2005): 1) slope belt, 2) fault step zone, 3) overburden zone, 4) footwall, 5) hanging wall, 6) the deep depression center, and finally 7) the shallow basin margin

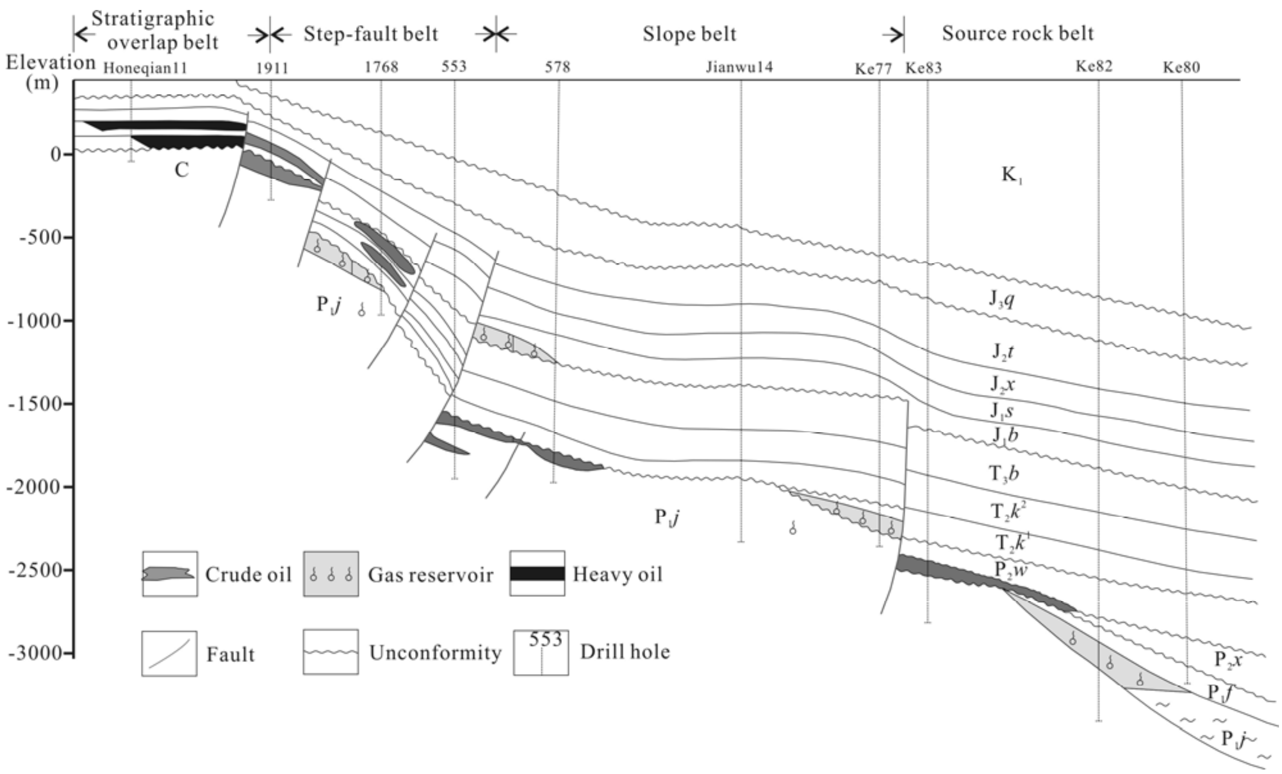

Fig. 3. Hydrocarbon accumulation model for the NW Junggar Basin (modified from Cao Jian et al., 2006).

(Fig. 3). The main hydrocarbon accumulation phases are: T_3–J_1, J_3–K_1 and K_2–E (Chen Jianping, 2002; Zhang Shanwen, 2013), followed by a small amount of oil and gas emission during the Himalayan period (Wu Yuanyan et al., 2002). However, there are different accumulation periods for various blocks across the PTB (Sui Fenggui, 2015). Oil and gas reservoirs in the fault zone mainly formed in the Triassic, whereas reservoirs in the overburden zone formed in the Yanshan period. There were two main reservoir formation stages in the slope belt, namely the Triassic and Yanshan.

2.3 Characteristics of the uranium mineralization

Sandstones in the middle–lower segments of Jurassic sediments mostly host uranium mineralization in the Xishanyao Formation (J_2x) (Lin Shuangxing, 1997). Uranium ore bodies, which exhibit stratified, tabular, complex roll, or hook-like shapes, strictly occur along the front of interlayer oxidation zones in the Xishanyao Formation (J_2x) (Lu Kegai, 2005). These ore bodies formed in zones between the yellow and gray–green sandstones (Fig. 4) (He Zhongbo et al., 2014), which are different from typical interlayer oxidation zone ore bodies situated between epigenetic oxidized yellow and primary gray sandstones (Charles., 1996; Wu et al., 2009). The thickness of uranium mineralization varies between 0.2 and 2.1m, and the uranium grade ranges from 0.01 to 0.033%. Ore-bearing rocks are gray–gray–green conglomerate sandstones, with minor purple, red, and yellow sandstone clumps or lenses (Lu Kegai, 2005). Oxidized sandstone is mainly yellow or light yellow, with a thickness which ranges from a few to tens of meters, buried to depths of less than 120m, on average from 49 to 116m (He Zhongbo et al., 2014). Tongue-shaped interlayer redox-oxidation fronts, developed along the Zaier Mountains, are concurrent with the Qigu Formation (J_3q) erosion line (Lu Kegai, 2005). All of these attributes indicate that both the age of uranium mineralization is younger than the surrounding host-rocks and mineralization was rapid.

Other uranium mineralization includes:

(a) A hydrocarbon reduction zone composed of greenish and gray–greenish rock belt that is 600–1500m wide and 3km long, developed within Jurassic sediments along the northern margin of NW-trending faults (Fig. 4a) (He Zhongbo et al., 2014).The greenish belt is not confined to specific strata, but corresponds to fracture and rock permeability. The greenish rock mainly consists of permeable rocks such as sandstone and conglomerate, a small amount of mudstone near the fracture, and a sand body with gray–green and variegated spots. From the margin to the central basin, the geochemical zoning in Jurassic sediments are characterized as the oxidation zone, partly oxidized zone, reduction zone and partly reduced zone (Fig. 4a), indicating that a significant relationship exists between uranium mineralization and the

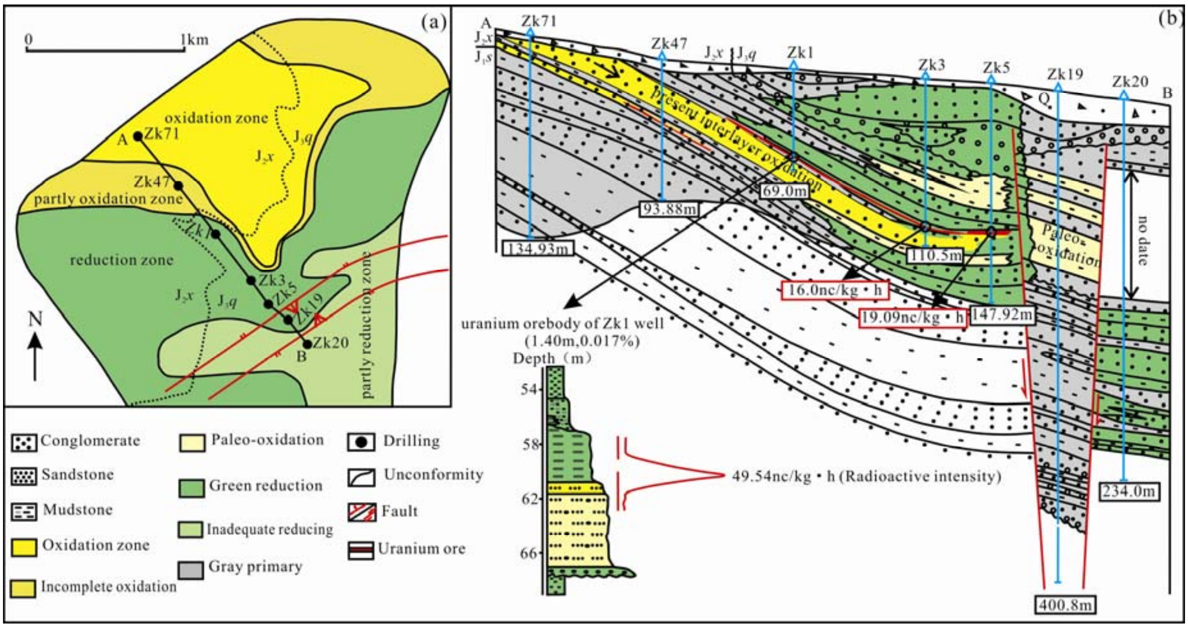

Fig. 4. Geochemical zoning and well cross-section of the Jurassic Xishanyao Formation in the NW Junggar Basin (modified from Lu Kegai, 2005).

hydrocarbon fluid (Chi Guoxiang et al., 2014). This is similar to observation described in previous studies from various regions globally such as the Dongshen uranium deposit in the Ordos basin (Cai et al., 2007) and other deposits in the word (Murray et al., 2010; Fuchs et al., 2015).

(b) The greenish altered sandstone has been charged and reduced by oil and gas, and is mostly characterized by a greenish and gray–greenish color. At the macroscopic scale, a large number of lumps, fine-grained, and fine veins of pyrite particles are visible. Some of this pyrite is associated with black oil spots in the sandstone (Fig. 2c) (Lu Kegai, 2005). Microscopic observation shows strong pyrite cementation in the greenish rock, small amounts of pitch veins (Fig. 2g), and numerous hydrocarbon fluid inclusions. And, surrounding clastic particles and cements have a light blue color (Fig. 2f). The above-mentioned characteristics indicate that the altered green sandstone was modified by hydrocarbon fluid at a certain time (Huang Shaohua et al., 2016; Liu et al., 2018).

(c) In the drill cores (ZK18, ZK20, ZK22, ZK52, and ZK53) (Fig. 4), the presence of red or yellow sandstones was observed and has been interpreted as partly reduced masses or lens (Fig. 4b), intercalated with the residual gray or gray–green conglomerates and sandstones (Lu Kegai, 2005). It has also been suggested that the timing of the first oxidation event was earlier than sandstone oil and gas reduction (He Zhongbo et al., 2014). Moreover, a pale -uranium anomaly, with a thickness of 5.2m and a gamma irradiation dose rate of 11.61nC/kg•h on average, was found in drill core ZK22.

(d) The existing interlayer oxidation zone formed from reactions between the modern oxidation water and the epigenetic reduction sandstone, in a process of oxidation-reduction-reoxidation (Lu Kegai, 2005). Uranium mineralization has been discovered in incomplete oxidation zones (Fig. 4). Lower wing uranium mineralization in drill core ZK47 was discovered, where the uranium mineralization body is located within the bottom yellow fine sandstone or mudstone, at a depth of 42.55–42.90m, a thickness of 0.35m, and a grade of 0.023%. In addition, the upper and lower uranium ore bodies wings are located in the lower sandstone of drill core ZK0001. The upper wing ore body developed in gray gravels, buried at depths of 98.30–99.30m, with a thickness of 1.00m, and a grade of 0.011%. The lower wing ore body is located at the bottom of the gravel layer, buried at a depth of 100.70–100.90m, with a thickness of 0.20m, and a grade of 0.012%. The oxide belt gradually appears in drill core ZK6 as well as the volume head uranium ore body. The ore body mostly occurs in the green gravel coarse sand rocks, buried at a depth that varies between 98.25 and 100.35m, with a thickness of 2.10m, and an average grade of 0.033% (Lu Kegai, 2005).

3 Sampling and Analytical Methods

In the Zaire Mountains and PTB region (altitudes ranging from 384 to 1345m a.s.l.), six outcrop samples (each weighing 2–3 kg), including granites (2), diorite (1), limestone (1), metamorphic sandstone (1), and Jurassic sandstone (1), were collected to reconstruct the low-temperature cooling history of the region (Fig. 1; Table 1). Apatite grains were separated from bulk samples by crushing, sieving, electromagnetic and heavy-liquids separation at Mineral Resources of Hebei Province in Langfang, China. Analyses were performed at the China University of Geosciences (Beijing), following the methods described in Yuan Wanming et al. (2007). Individual apatite grains were mounted in epoxy resin on glass slides, and then ground and polished to an optical finish to expose internal grain surfaces. Spontaneous tracks were etched in 7% HNO_3 at 25ºC for 30 s. All samples were neutron flux irradiated in a well-thermalized 421 reactor at the China Institute of Atomic Energy in Beijing (Chen et al. 2015). U-poor muscovite was used as an external detector, along with the glass standard, CN5, for neutron dosimetry. After irradiation, the muscovite was etched with 40% HF for 20 min at 25ºC to reveal the induced fission tracks (Roman et al., 2015). Fission-track densities, in both natural and induced fission-track populations, were measured in air at 100×15 magnification. Only crystals with prismatic sections parallel to the crystallographic c-axis were analyzed when possible (Zhang Beihang et al., 2017). Fission track ages were calculated using the IUGS-recommended zeta calibration approach, and results were quoted with $\pm 1\sigma$ standard error (Paulo et al., 2015; Qi et al., 2016). The weighted mean zeta value for apatite used by the fission-track operator was 386.8±18.1a/cm^2, according to sample standard calibration (Chen et al., 2015). Analytical results are given in Table 1. Eleven additional samples from previous studies are also incorporated in this study (Li Wei, 2007; Li Li et al. 2008; Li Zhenhua, 2011). The analyzed results of 17 samples are presented in Table 1 and Fig. 1.

Analyses were subjected to the χ^2 test to detect whether the data sets contained extra-Poissonian error (Silvia et al., 2014). A probability >5% is indicative of a homogenous population, and the pooled age is used as the age estimate of the sample. A χ^2 probability of less than 5% denotes a significant spread of single grain ages, and therefore, the central age (the weighted mean age) is used.

Based on FT parameters (i.e., ages and lengths), the geological setting of Mesozoic–Cenozoic evolution, the cooling history of the different regions (Franco et al., 2011; Sui Fenggui, 2015), and the temperature-time (T-t) path for each sample was modeled using the HeFTy software (version1.6.7; Ketcham, 2009) and the multi-kinetic annealing algorithm from Ketcham et al. (2007). The analytical conditions were controlled for inversion modeling by restricting (1) all tracks initially formed being able to be completely annealed in the case of high temperatures (>110ºC, greater than total annealing) and

Table1 Apatite fission-track results of the NW Junggar Basin

Sample	Elevation (m)	Location	Rock type	Era	Grain numbers (n)	ρ_s (10^5/cm^2) (N_s)	ρ_i (10^5/cm^2) (N_i)	ρ_d (10^5/cm^2) (N_d)	$P(\chi^2)$ (%)	Central Age (Ma) ($\pm 1\sigma$)	Pooled Age (Ma) ($\pm 1\sigma$)	Mean length L(μm) ($\pm 1\sigma$) (N)
*ZX1	1510	N45°31′17.2″ E83°50′56″			23	1.612 (175)	4.043 (439)	8.826 (10438)	99.7	67±6	67±6	12.1±2.2 (104)
*D480/1	1496	N45°43′55.5″ E83°32′37.8″			22	2.155 (238)	4. 618 (510)	8.723 (10438)	94.8	78±7	78±7	11.7±2.2 (59)
*D480/2	1563	N45°42′54.4″ E83°33′33.3″			23	3.526 (245)	7.340 (510)	8.620 (10438)	31. 7	81±8	79±7	11.5±1.3 (20)
*D480/3	1805	N45°35′14.7″ E83°39′03.6″			25	2.368 (446)	4.247 (800)	8.517 (10438)	62.9	91±6	91±6	12.5±2.5 (106)
*D480/4	1398	N45°30′46.4″ E83°56′23.1″			23	3.759 (732)	5.038 (981)	8.517 (10438)	94.6	121±7	121±7	13.6±1.9 (113)
*DZX2	617	N45°41′53.9″ E84°55′29.6″	Granite		24	2.241 (448)	2. 991 (598)	8.620 (10438)	96. 6	123±9	123±9	13.6±2.1 (101)
*D468/1	732	N45°42′40″ E84°50′42″		Carboniferous	21	13.113 (1704)	17.992 (2338)	8.723 (10438)	15. 1	120±6	121±6	12.4±1.6 (105)
※Z28-1	680	/			10	2.580 (160)	85.20 (528)	15.01 (3762)	8.6	74.8±12.2	/	12.0±0.5 (28)
※Z28-2	670	/			21	1.820 (206)	57.30 (647)	15.08 (3779)	0.8	73.0±10.0	/	13.5±0.5 (21)
Z12-01	1345	N45°31′34.98″ E83°59′18.53″			28	3.294 (384)	16.555 (1930)	14.59 (7380)	0	57±7.2	56±4.1	12.1±2.1 (102)
Z12-02	1280	N45°32′19.31″ E84°03′09.23″			24	1.978 (388)	8.206 (1610)	14.787 (7380)	2.79	70±6.1	69±5.1	13.3±2.0 (54)
Z12-03	384	N45°54′23.76″ E85°16′09.45″	Diorite		28	2.1 (415)	5.744 (1135)	15.577 (7380)	8.0	110±9.1	109±8.2	12.7±1.9 (101)
Z12-04	694	N46°00′20.13″ E84°57′07.57″	Limestone		30	5.176 (346)	9.245 (618)	9.162 (7380)	88.5	98±8.2	98±8.1	12.9±1.7 (91)
Z12-05	1135	N45°34′44.01″ E84°12′33.33″	Meta-sandstone	P_1	28	1.581 (214)	4.189 (567)	14.392 (7380)	97.0	104±9.8	104±9.8	13.2±2.3 (68)
Z12-06	562	N45°38′40.58″ E84°47′22.24″		J_1b	28	2.917 (1166)	7.01 (2802)	15.281 (7380)	26.7	121±7.6	122±7.2	13.4±1.8 (101)
▽DLS-01	/	/	Sandstone	J_1s	28	4.04(1232)	6.887 (2100)	9.805 (10322)	25.2	108±6	110±5	12.8±1.7 (105)
▽DLS-02	/	/		K_1tg	27	3.536(642)	6.648 (1207)	9.917 (10322)	71.2	101±6	101±6	12.6±1.6 (103)

Note: For sample location see Fig. 1. ρ_s is the spontaneous fission track density; N_s is the number of spontaneous fission tracks counted; ρ_i is the induced fission track density; N_i is the number of induced fission tracks counted; ρ_d is the induced dosimeter glass CN5 fission track density; N_d is the number of induced dosimeter glass CN5 fission tracks counted; $P(\chi^2)$ is the chi-square probability; L is the mean confined fission track length.
* from Li Wei (2007), ※ from Li Li et al. (2008), and ▽ from Li Zhenhua (2011).

old ages (older than the oldest single grain age), (2) the AFT partial annealing zone (PAZ) temperature range of 60–110ºC and the AFT pooled age, and (3) lower temperatures between 20 and 60ºC and the youngest pooled age (approximately 20 Ma). In the modeling, the Kolmogorov-Smirnov test was employed to assess the fit between the modeled and measured track length distributions (Chen et al., 2015). Inversion modeling was performed with 10,000 randomly chosen time-temperature (t–T) histories for each sample, such that sufficient model paths were available to clearly differentiate between "good fit" and "acceptable fit" solutions (cf. Ketcham, 2005 for details and definitions of "good" and "acceptable" fits).

4 AFT Results and Thermal History Modeling

4.1 AFT data and discussion

The $P(\chi^2)$ value is used to evaluate the probability of whether a single particle belongs to the same age group (Roman et al., 2015). When $P(\chi^2)$ is greater than 5%, the age belongs to the same age group. However, if the $P(\chi^2)$ probability is less than 5%, counted grains represent a mixed age population with real age differences between single grains (Lin et al., 2015). The AFT analytical results are listed in Table 1. The $P(\chi^2)$ values for two samples (Z12-01 and Z12-02) are 0 and 2.79, respectively, indicating that these two samples have a significant spread in single-grain ages (Fig. 5). The other four samples (Z12-03, Z12-04, Z12-06, and Z12-07) all pass the χ^2 test with a $P(\chi^2)$ value that is well over 5%, indicating that single-grain age distribution is consistent with a single age population in each sample, which is also similar to their central age such that these pooled ages represent the tectonothermal event (Zhang Beihang et al., 2017). The six new samples yielded a relatively wide spread in AFT ages, ranging from 57±7.2 to 122±7.2 Ma, consistent with ages of 67±6 to 123±9 Ma previously published (Table 1). All samples have younger AFT ages than the crystallization or deposition ages. This pattern indicates that samples experienced post-formation thermal events within the apatite PAZ. Moreover, there is no occurrence of volcanic or hydrothermal activity in the NWJB, and all the samples are far from the fault zone. We therefore interpret that these ages represent cooling ages, which could indicate regional denudation events (Qi et al., 2016). All samples have two peak ages, indicating two tectonic episodes in the Yanshanian movement (Bai Guojuan, 2009; Li Zhenhua, 2011).

The confined track-length distributions of the samples show unimodal patterns and asymmetrical near normal distribution characteristics (Fig. 6), with the MTL ranging from 12.1±2.1 (sample Z12-01, N=102) to 13.4±1.8 μm (sample Z12-06, N=101), which are neither shorter than the initial TL of 16.3±0.9μm, nor shorter than the TL of 14.5–15.5μm, indicating that most samples experienced both long-term partial annealing and slow cooling (Du Zhili et al., 2007). This result suggests that the NWJB has a slow cooling history, rather than a complex uplift

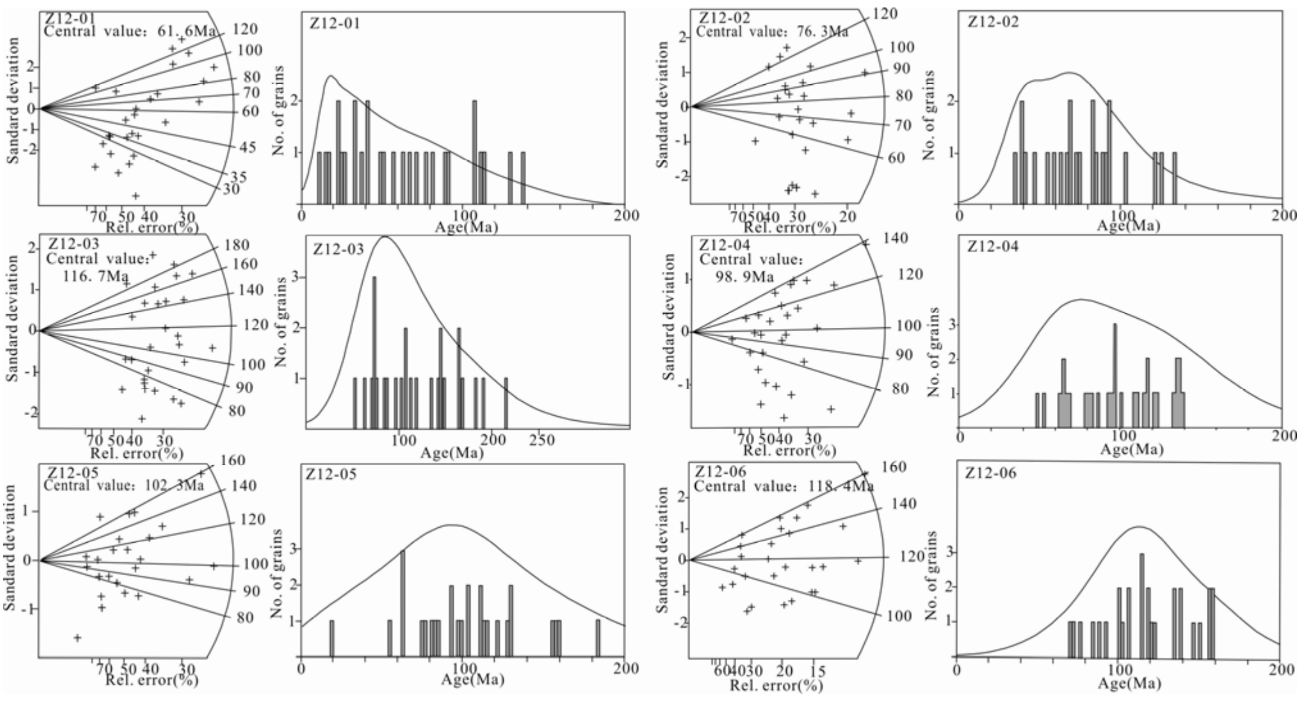

Fig. 5. Single particle age and radar diagrams of apatite fission tracks in the NW Junggar Basin.

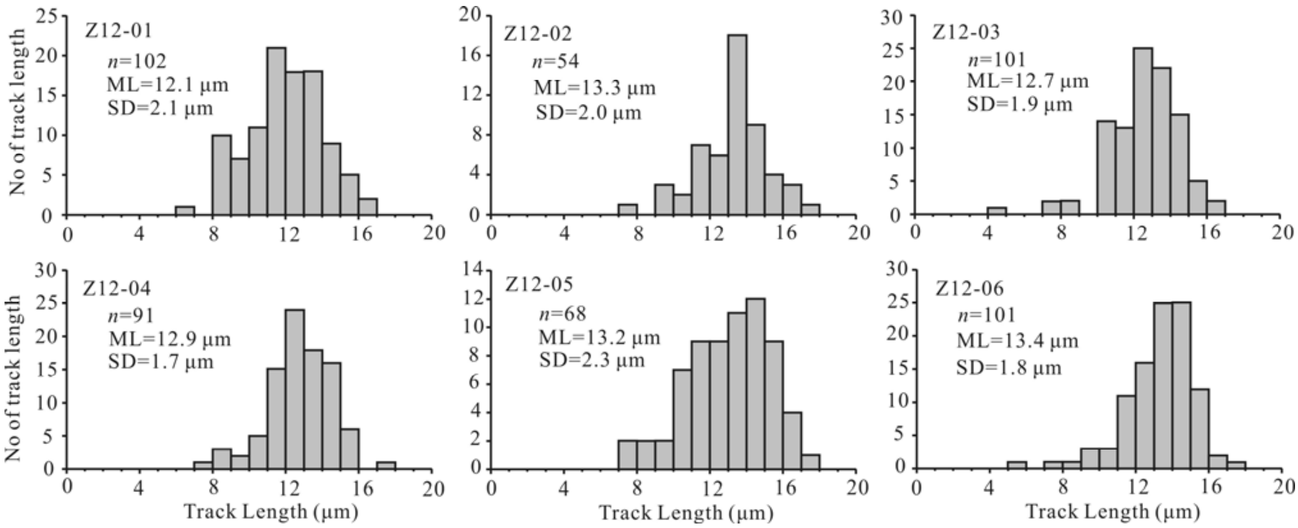

Fig. 6. Traditional fission track length histograms for NW Junggar Basin.

history.

Generally, samples from high altitude with older FAT ages passed through the PAZ earlier than samples from low altitudes (Fig. 1) (Silvia et al., 2014; Paulo et al., 2015). However, there is no significant correlation between FAT ages and altitude, or between track-length and altitude (Table 1), indicating that there are variation of the uplift times and rates in the different units (Lin et al., 2015). Regardless of this dispersion, however, samples from northwest of the Daerbute fault have ages ranging from 57±7.2 to 121±7 Ma, where most are younger than 100 Ma, except for sample D480/4 and Z12-05, which have ages of 121±7 and 104±9.8 Ma, respectively. These ages are significantly younger than samples to the southeast of the fault, where all ages are greater than 100 Ma. These results describe a trend where FAT ages become younger toward the southeastern regions of the study area. This may have resulted from the upward thrusting of the orogenic belt into the basin due to northwestward extrusion during the late Yanshanian period, as previously suggested (He Dengfa et al., 2004; Li Wei, 2007). Thus, it seems that tectonic uplift initiated in the northwest and propagated to the southeast in my study area.

4.2 Thermal modeling: *t-T* paths

To quantify the inferred differences in cooling history between the various tectonic zones sampled, the track-length distributions of six samples were inverted to investigate their thermal histories (Fig. 7). Moreover, the uplift rates and sample evolution from initial uplift to their present stage was calculated (Table 2). The AFT closure temperature is 110ºC, the late Jurassic Paleogene temperature gradient is 28.4ºC/km, the late Cretaceous Paleogene temperature gradient is 24.8ºC/km, the Paleogene is 22.6ºC/km (similar to the present day average geothermal gradient), and the present surface temperature is 18.4ºC (Qiu Nansheng et al., 2002).

Sample Z12-01, from the western border of the Daerbute fault, exhibits a three stage thermal history with fast initial cooling at 1.5–2ºC·Ma^{-1} during the late Cretaceous (ca. 80–60 Ma), a prolonged history of slow, continuous cooling from ca. 60 Ma onward, which was followed by very rapid (3–4ºC·Ma^{-1}) cooling again during the last 15–20 Ma. The uplift extent of these three stages is 1056, 528, and 1641m, respectively, and the uplift rates were 0.053, 0.012, and 0.109 mm·a^{-1}, respectively. Sample Z12-02, at the same locality, shows a rapid uplift history at 0.070mm·a^{-1} from 80–55 Ma, with a possible slow cooling rate of 0.027 mm·a^{-1} since ca. 55 Ma.

The northern border of the Zaier Mountains, represented by samples Z12-03 and Z12-04, also has a distinct three stage cooling history with initial rapid cooling at 1–2ºC·Ma^{-1} since ca. 140 Ma, possible thermal stability from ca. 90 to ca. 20 Ma, immediately followed by extremely rapid cooling of ca. 1.5ºC·Ma^{-1} since ca. 20 Ma. This cooling history is similar to that of sample Z28-18 (Li Li et al., 2008), and samples DZX/1 and D480/1 (Li Wei, 2007), although modeling approaches in these studies are slightly different. Sample Z12-05 exhibits three stage continuous cooling with a relatively slow initial rate of ca. 0.5ºC·Ma^{-1} since ca. 130 Ma with a possible acceleration to 1.5ºC·Ma^{-1} since ca. 60 Ma, which was then followed by a steady state from ca. 50 Ma to present. Li Wei (2007) also modeled a similar cooling history for samples D480/4 and DZX2. Sample Z12-06, from the PTB, exhibits a two stage cooling history, with relatively fast (ca. 1ºC·Ma^{-1}) cooling from ca. 140 to ca. 40 Ma followed by a late phase of very slow (ca. 0.1ºC·Ma^{-1}) cooling since ca. 40 Ma. The uplift rate is 0.032 mm/a and 0.006 mm/a,

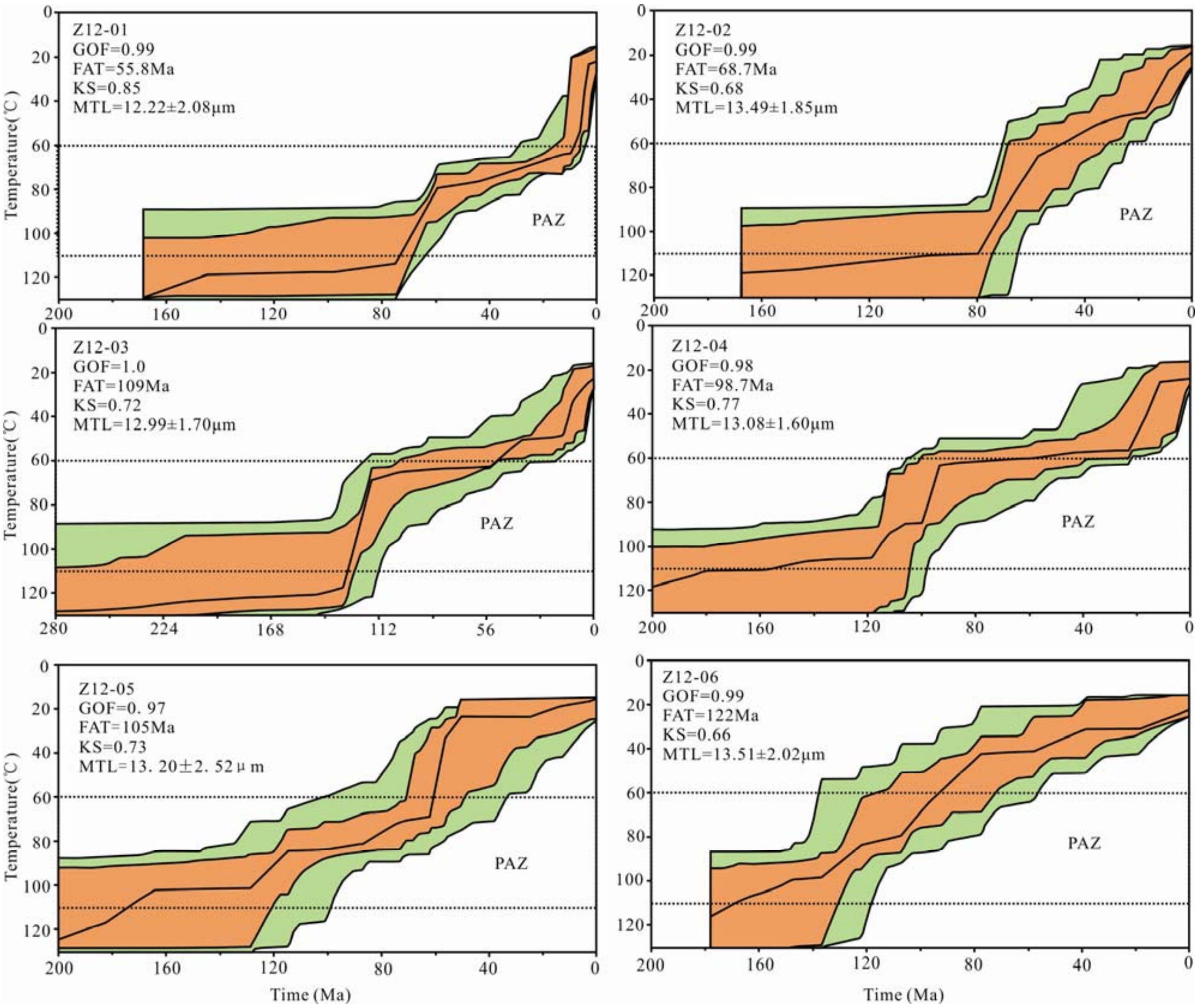

Fig. 7. *t*-*T* modeling results for the six samples shown as path envelopes encompassing the thermal histories that generated a good (purple shading) and acceptable fit (green shading) with the data.

Table 2 Uplift range and rate for samples in different stages of the NW Junggar Basin

Sample	Stage 1	Uplift range (m)	Uplift rate (mm/a)	Stage 2	Uplift range (m)	Uplift rate (mm/a)	Stage 3	Uplift range (m)	Uplift rate (mm/a)
Z12-01	80–60 Ma 110–80ºC	1056	0.053	60–15Ma 80–65ºC	528	0.012	15–0 Ma 65–18.4ºC	1641	0.109
Z12-02	80–55 Ma 110–60 ºC	1761	0.070	55–0Ma 60–18.4ºC	1465	0.027	/	/	/
Z12-03	140–105 Ma 110–65ºC	1585	0.045	105–20 Ma 65–45ºC	704	0.008	20–0 Ma 45–18.4ºC	937	0.047
Z12-04	120–80Ma 110–65ºC	1585	0.040	80–20 Ma 65–50ºC	528	0.009	20–0 Ma 50–18.4ºC	1113	0.056
Z12-05	120–80 Ma 110–80ºC	1056	0.026	80–40 Ma 80–25ºC	1937	0.048	40–0 Ma 25–18.4ºC	232	0.006
Z12-06	135–40 Ma 110–25ºC	2993	0.032	40–0 Ma 25–18.4ºC	232	0.006	/	/	/

respectively.

The modeled sample thermal histories from the WJOB are characterized by a three stage rapid cooling, which are early Cretaceous (ca. 140–115 Ma), late Cretaceous (ca. 80–60 Ma), and Miocene–present (since ca. 20 Ma). However, samples from the PTB show only rapid cooling during the late Yanshanian period and a late stage of extremely slow uplift in the Himalaya period.

5 Discussions

Within the basin, hydrocarbon migration and uranium mineralization were controlled by tectonic activity (Chen et al., 2011; Bonnetti et al., 2017; Liu Zhangyue et al., 2016, 2017). Generally, oil and gas reservoirs are located within the interior of the basin. Sandstone type uranium deposits are generally epigenetic ore deposits, and occur mostly along the margins of Mesozoic–Cenozoic basins in which uranium-rich, oxygen-bearing interlayer water seeps through the host sandstone (Wu et al., 2009). Continuous or episodic invasion of the reduced rock by oxygenated ground waters resulted in continuous or episodic solubilization and precipitation of uranium and redox interface migration into the paleodip (Yang et al., 2014; Bonnetti et al., 2014). The recycling process may enrich the ore-grade uranium at the redox front (integrated geochemical barrier) (Charles, 1996; Michel, 2010). Furthermore, hydrocarbons not only provide secondary/ epigenetic reducing agents (i.e., CH_4, CO, H_2S) for uranium precipitation (Cai Yuwen et al., 2017), but also protect the formed uranium ore bodies (Cai et al., 2007; Chi et al., 2014; Liu et al., 2018; Fuchs et al., 2015). Hydrocarbon accumulation and strong tectonic activity simultaneously occurred during a relatively short period (Hu Yang et al., 2012), whereas sandstone U-ore formed during a long era of tectonic stability (Landais., 1996; Michel, 2010), and later strong tectonic movement (Chen et al., 2011). Based on AFT analysis, field geological surveys, and previous studies, the coupling relationship between tectonic uplift, hydrocarbon migration, and uranium mineralization in the NWJB are discussed in this study (Fig. 8).

Previous studies indicate that the middle–lower Jurassic coal-bearing formation is the prospecting target layer for sandstone-type uranium deposits (Lin Shuangxing, 1997; Feng Shirong, 1998). In general, the uranium metallogeny is explainable in terms of oxidation–reduction reactions, which control uranium transport (in oxidized conditions) and deposition (in reduced conditions) (Landais, 1996). The Middle–Lower Jurassic sandstone rich in organic matter and pyrite has a higher reduction capacity (Lin Shuangxing, 1997; Huang Shaohua et al., 2016). Thus, the above-mentioned matters will induce abundant reductant for epigenetic uranium mineralization (Charles., 1996; Bonnetti et al., 2014). When considering the tectonic and paleoclimatic evolution in the area, the depositional break between the Xishanyao (J_2x) and Toutunhe (J_2t) formations lasted 4–10Ma and the denudation thickness is 100–340m (He Dengfa et al., 2007; Zhang Shanwen et al., 2013). Meanwhile, the NWJB's tectonic and paleoclimatic environment changed from J_2x to J_2t. The J_2x Formation was deposited in a weakly extensional tectonic environment and warm and moist paleoclimate, while the J_2t Formation was deposited in a weak extruding tectonic environment and a hot and dry palaeoclimate (Bai Guojuan, 2009). Therefore, the middle-lower Jurassic formations in the PTB had an opportunity to be uplifted to the surface, and accept shallow water infiltration and transformation with oxygen and uranium (Bonnetti et al., 2014, 2017). This eventually resulted in the formation of interlayer oxidation zones and paleo-uranium ore bodies (Fig. 8).

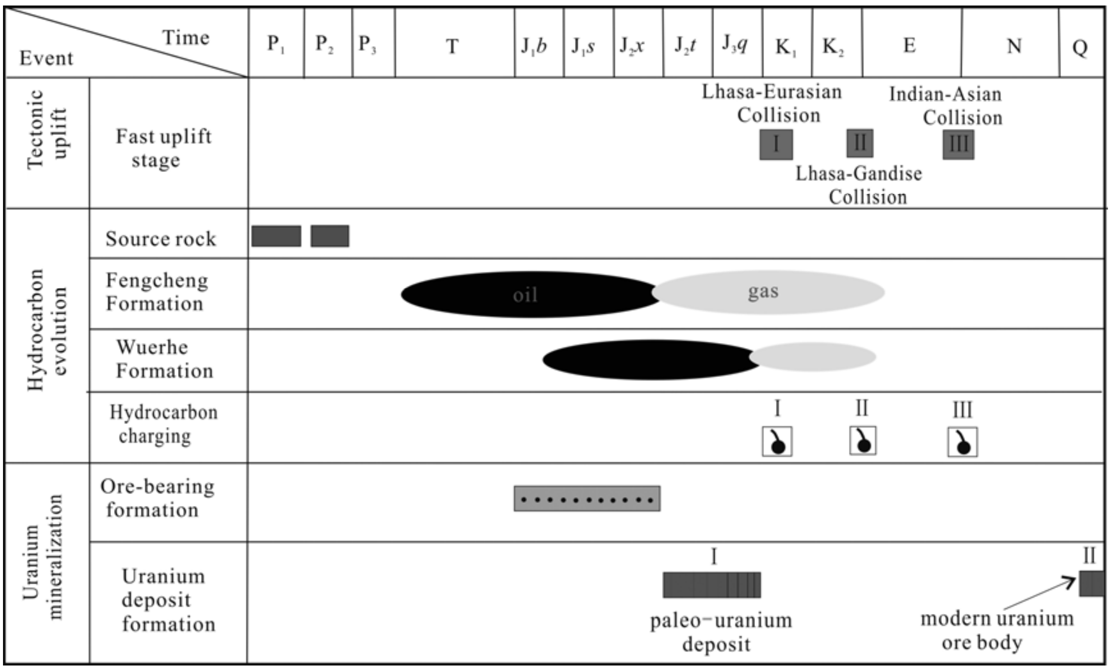

Fig. 8. Coupling relationships between tectonic uplift, hydrocarbon charging, and uranium mineralization in the northwestern margin of Junggar Basin.

5.1 Stage 1: Early Cretaceous

Thermal history modeling of samples Z12-03 and Z12-04 reveal rapid uplift in the WJOB during K_1 (Fig. 7), which corresponds to the second episode of Yanshanian regional tectonic movement (Fig. 8) (Du Shekuan, 2004; Franco et al., 2011), i.e., a response to the collision between the Lhasa and Eurasian Blocks along the Bangong Co-Nujiang Suture from 140–125 Ma (Li Li et al., 2008). Intense tectonic activity led to the extensive distribution of Cretaceous basal conglomerates and their regional unconformities, with the underlying strata, in the PTB (Li Zhenhua, 2011; Zhang Shanwen, 2013), as well as fault structure reactivation that eventually provided paths and power for petroleum migration (Allen et al., 1997). A critical hydrocarbon pooling event occurred in the study area during this period (Table 3; Fig. 8), when deep hydrocarbon pools formed from P_1f source rocks during T_3–J_1, and were disrupted and dissipated, which initiated the formation of secondary pools (Sui Fenggui, 2015; Chen Jianping et al., 2016). The P_2w source rocks entered an extensive hydrocarbon-generating and expulsion stage, forming primary pools (Fig. 8).

Extensive hydrocarbon invasion also resulted in initial reductive inundation and protection of the large-scale paleo-interlayer oxidation belt and paleo-uranium ore bodies, rendering mineral exploration more difficult (He Zhongbo et al., 2014; Huang Shaohua et al., 2016). Similar to roll-front uranium deposits along the Texas Coastal Plains (USA) (Richard et al., 1978), geochemical trends developed during early mineralization processes may have been modified by later secondary host beds reduction (Cai et al., 2007). In the study area, reductant introduction during post mineralization (i.e., hydrocarbon) from buried oil and gas accumulations may also have reduced altered tongue, and, therefore, disrupted primary redox boundaries established during the ore-forming stage. Field investigation shows that yellow ellipsoidal paleo-oxidation lenses are wrapped in the Badaowan Formation black oil sandstone with a major axis of 1.8 m and a minor axis of 0.5 m (Fig. 2b). The primary gray mudstone already oxidized to a yellow color in the drill hole cross section (Lu Kegai, 2005), which implies the possible occurrence of epigenic oxidation and uranium mineralization before hydrocarbon invasion. Therefore, the occurrence of very intense paleo-oxidation during the late Jurassic–early Cretaceous period consequently led to high ore-grade uranium mineralization, which means a significant potential for the formation of paleo-uranium deposits. On the other hand, large-scale lacustrine invasion occurred during the early Cretaceous in the PTB (Fig. 2a) (He Zhongbo et al., 2014). Thus, lower Cretaceous mudstones quickly covered the middle and lower Jurassic Formation after oil and gas recharge. Shallow oxidizing water did not affect that Jurassic target Formation, and therefore, did not suspend epigenetic oxidation and uranium mineralization.

5.2 Stage 2: Late Cretaceous

Thermal history modeling of samples Z12-01 and Z12-02 reveal a rapid uplift event in the WJOB during K_2 (Fig. 7), which corresponds to Kohistan Dras Island Arc regional overgrowth (Fig. 8) (Li Wei, 2007; Li Zhenhua, 2011). This is a response to the collision between the Gandise and Lhasa Blocks during the late Cretaceous (Du Shekuan et al., 2007; Yuan Wanming et al., 2007). Intense tectonic uplift led to regional unconformities between the Cretaceous and overlying strata in the PTB (He Dengfa et al., 2007; Bai Guojuan, 2009), as well as a further disruption to regional deep hydrocarbon pools (Fig. 8) (Wang Huimin et al., 2005). The resulting extensive hydrocarbon migration produced secondary Mesozoic high oil pools or tar sands (Fig. 2c), which extended until dissipation into the aerosphere (Wu Yuanyan et al., 2002; Shen Yang et al., 2015). Late Cretaceous deposits rarely developed during stages of slow PTB uplift. The Middle–Lower Jurassic sandstone target formation was overburdened by lower Cretaceous mudstone aquifuges and sheltered by multiple hydrocarbon injections (He Zhongbo et al., 2014). This further prevented the target formation from restructuring via overlying oxygen and uranium-bearing strata, and thus, uranium mineralization was suspended throughout this period.

Table 3 Oil source and filling periods of the NW Junggar Basin

Oil field	Reservoir	Source rock	Oil generation period	Oil charging period	Data source
Hongshanzui	J_1b, J_3q	P_1f, P_2w	T_3–J_3, J_1–K_1	J_3–K_1	Zhang Shanwen, 2013
Keramay	J, K	P_1f	T_3–J_3	J_3–K_1 (150–125 Ma), K_2–E	Chen Jianping, 2002
	C, P, T	P_1f, P_2w	T_3–J_3, J_1–K_1	T_3–J, K_2–E	Sui Fenggui, 2015
	T_1b, T_2k	/	/	T_3–J, J_{1-2}	
Chunhun	J_1b, K	P_1f	T_3–J_3	J_3–K_1, K_2–E	Zhang Shanwen, 2013; Sui Fenggui, 2015
	C, P	P_1f	T_3–J_3	T_3–J, J_{1-2}, K_2–E	
Alade	T_1b, T_2k, J_2x, K	P_1f	T_3–J_3	K_2–E	
Wuerhe	T_1b, T_2k	P_1f, P_2w	T_3–J_3, J_1–K_1	T_3–J, K_2–E	
	J, K	P_1f	T_3–J_3	K_1 (136–130 Ma), K_2–E	Bai Guojuan, 2009; Li Zhenhua, 2011; Shen Yang et al., 2015
Fengcheng	J_1b, J_3q	P_1f, P_2w	J_3–K_1, J_1–K_1	J_3–K_1	Zhang Shanwen, 2013

5.3 Stage 3: From Miocene onward

Thermal history modeling of samples Z12-01 and Z12-02 (Fig. 7) also reveal another rapid uplift event in the WJOB mountains from the Miocene onward, representing a remote response to the Indian-Asian Collision since 55 Ma (Fig. 8) (Du Zhili et al., 2007; Hu Yang et al., 2012; Muhammad et al., 2016). This resulted in the reactivation of local fault structures that involved strike-slip deformation (Shao Yu et al., 2011; Guo Zhaojie et al., 2017). This evidence comes from strike-slip faults and Q formations detected during field surveys (Fig. 2d), and are considered as another disruption to existing hydrocarbon pools (Fig. 8) (Wu Yuanyan et al., 2002). The seven NE-trending asphalt veins (perpendicular to the faults) found in the Cretaceous Tuguluqun strata (K_1*tg*), for example, formed when hydrocarbon infiltrated strata along the faults (Shen Yang et al., 2015). Previous studies have also demonstrated that Himalayan tectonic movement had minimal impact, which provided satisfactory conditions for the preservation of PTB hydrocarbon pools (Sui Fenggui, 2015). Thermal history modeling of sample Z12-06 also confirms the presence of minimal tectonic activity and constant uplift at a low speed throughout Himalayan movements (Fig. 7). While PTB uplift was a little faster during this period (Fig. 4), the overall rate was still low. The target layer was still covered by overlying strata for a significant period of time in the Cenozoic, and had not yet undergone mineralization or transformation from oxygenated uranium bearing water (Lu Kegai, 2005). As a result, with the gradual erosion of overlying strata, the hydrocarbon-exposed Middle–Lower Jurassic target formation begin to outcrop at the surface and transform via overlying oxygen-bearing water until the Quaternary. This led to uranium mineralization in the Jurassic Karamay sandstone (Fig. 8), which is frequently located between the green hydrocarbon-reducing sandstone and yellow sandstone (Fig. 4) (He Zhongbo et al., 2014; Chi Guoxiang et al., 2014). The uranium ore bodies, however, are low grade and have small sizes as a result of short duration ore forming processes, insufficient uranium and oxygen-bearing groundwater recharge, and slow interlayer oxidation belt development. Because the uplift is different for the various regions, Jurassic strata, in most parts of the PTB are still not exposed, and oxidation time in several regions (i.e., the Karamay region) is short. Therefore, the metallogenic potential of this stage is relatively small.

6 Conclusions

The tectonic thermal uplift history of the NWJB was inversely modeled by AFT thermochronology. These results indicate that:

(1) All sample AFT ages fall into the range of 56±4.1 to 122±7.2Ma, which are much younger than local rocks or strata. The average track length was medium to short at 12.1±2.1 to 13.4±1.8μm and unimodal. The samples record a continuous, single cooling event, and a relatively slow uplift processes since the Cretaceous.

(2) The uplift process in the NWJB varied from one place to another: uplift in the southeast began later than that in the northwest, suggesting a fault system post spread -thrust nappe into the basin in the late Yanshanian. Thermal history modeling yielded three episodes of rapid uplift in the WJOB mountains during the early Cretaceous, late Cretaceous, and from the Miocene onward, which were responsible for regional unconformities along the J_3/K_1, K_2/E and E/N, and three large-scale hydrocarbon injection events in the PTB, respectively.

(3) Hydrocarbon injection during the early Cretaceous, in particular, resulted in the initial inundation and protection of the paleo-uranium ore bodies that formed during the Middle–Late Jurassic. The uplift and denudation of the PTB was extremely slow from 80 Ma onward, and slight influenced by Himalayan movement. However, uplift was faster from the Miocene onward, which caused the target formation to outcrop at the surface again during the Quaternary. Then, the hydrocarbon-reduced sandstone was subjected to the oxidation of oxygen and uranium-bearing water, which led to the present-day uranium ore bodies.

Acknowledgements

This study is jointly conjugal supported by the Nuclear energy development project (grant No. H1142) and Nation Pre-research Project (grant No. 3210402). The authors would like to thank geology party No. 216 of CNNC for providing much useful data. We are also very grateful to anonymous reviewers for their constructive and thorough reviews of the manuscript.

Manuscript received Aug. 24, 2017
accepted Jan.17, 2018
edited by Hao Qingqing

References

Allen, M.B., and Vincent, S., 1997. Fault reactivation in the Junggar region, northwest China: the role of basement structures during Mesozoic–Cenozoic compression. *Geological Society London Special Publications*, 154: 151–155.

Bai Guojuan, 2009. *The tectonic feature and hydrocarbon accumulation in the northwest part of Junggar Basin*. Xi'an: Northwest university (master thesis): 10–74 (in Chinese with English abstract).

Bonnetti, C., Cuney, M., Bourlange, S., Deloule, E., Poujol, M., Liu, X.D., Peng, Y. B., and Yang, J.X., 2017. Primary uranium sources for sedimentary-hosted uranium deposits in NE China: insight from basement igneous rocks of the Erlian Basin. *Miner Deposita*, 52(3): 297–315.

Bonnetti, C., Malartre, F., Huault, V., Cuney, M., Bourlange, S., Liu, X.D., and Peng, Y.B., 2014. Sedimentology, stratigraphy and palynological occurrences of the Late Cretaceous Erlian Formation, Erlian Basin, Inner Mongolia, People's Republic of China. *Cretaceous Research*, 48: 177–192.

Cai Yuwen, Zhang Shuichang, He Kun, Mi Jingkui, Zhang Wenlong, Wang Xiaomei, Wang Huajian and Wu Chaodong. 2017. Effects of U-ore on the chemical and isotopic composition of products of hydrous pyrolysis of organic matter. *Petroleum Science*, 14(2): 315–329.

Cai, C.F., Li, H.T., Qin, M.K., Luo, X.R., Wang, F.Y., and Ou, G.X., 2007. Biogenic and petroleum-related ore-forming processes in Dongsheng uranium deposit, NW China. *Ore Geology Reviews*, 32(1): 262–274.

Cao Jian, Hu Wenxuan, Yao Suping, Zhang Yijie, Wang Xulong, Zhang Yueqian and Tang Yong, 2006. Evolution of petroleum migration and accumulation in the northwestern margin of the Junggar Basin: fluid inclusion geochemistry. *Geological Review*, 52(5): 700–706 (in Chinese with English abstract).

Chang, J., Qiu, N.S., and Li, J.W., 2012. Tectono-thermal evolution of the northwestern edge of the Tarim Basin in China: constraints from apatite (U–Th)/He thermochronology. *Journal of Asian Earth Sciences*, 61: 187–198.

Charles, S.S., 1996. The roles of organic matter in the formation of uranium deposits in sedimentary rocks. *Ore Geology Reviews*, 11(s1–3): 53–69.

Chen Jianping, 2002. Hydrocarbon migration satges and accumulation in Karamay oilfield, Junggar Basin. *China offshore Oil and Gas* (Geology), 16(1): 19–22 (in Chinese with English abstract).

Chen Jianping, Wang Xulong, Deng Chunping, Liang Digang, Zhang Yueqian, Zhao Zhe, Ni Yunyan, Zhi Dongming, Yang Haibo and Wang Yutao, 2016. Oil and gas, occurrence petroleum system in the Junggar Basin, Northwest China. *Acta Geological Sinica*, 90(3): 421–450 (in Chinese with English abstract).

Chen Zhengle, Liu Jian, Gong Hongliang, Zheng Enjiu, Wang Xinhua and Pan Jinhua, 2006. Cenozoic Tectonic Movement and its Control on Sandstone-type Uranium Deposits in Northern Junggar Basin. *Acta Geologica Sinica*, 80(1): 101–111 (in Chinese with English Abstract).

Chen Zhengle, Lu Kegai, Wang Guo, Chen Bolin, Wang Guorong, Zheng Enjiu, Cui Lingling and Ding Wenjun, 2010. Characteristics of Cenozoic structural movements in southern margin of Junggar Basin and its relationship to the mineralization of sandstone-type uranium deposits. *Acta Petrologica Sinica*, 26(2):457–470 (in Chinese with English abstract).

Chen, H., Hu, J.M., Wu, G.L., Shi, W., Geng, Y.G., and Qu, H.J., 2015. Apatite fission-track thermochronological constraints on the pattern of late Mesozoic–Cenozoic uplift and exhumation of the Qinling Orogen, central China. *Journal of Asian Earth Sciences*, 114: 649–673.

Chen, Z.L., Liu, J., Gong, H.J., Han, F.B., Stephanie, M.B., Zheng, E.J., and Wang, G., 2011. Late Cenozoic tectonic activity and its significance in the Northern Junggar Basin, Northwestern China. *Tectonophysics*, 497(1): 45–56.

Chi Guoxiang and Xue Chunji, 2014. Hydrodynamic regime as a major control on localization of uranium mineralization in sedimentary basins. *Science China Earth Sciences* (English Edition), 57(12): 2928–2933.

Du Shekuan, 2004. *Research on the foreland thrust belt and on the accumulation of petroleum in the north-western margin of the Junggar Basin, China*. Beijing: Chinese Academy of Geological Sciences (Ph. D thesis): 13–122.

Du Zhili and Wang Qingchen, 2007. Mesozoic and Cenozoic uplifting history of the Tianshan region: insight from apatite fission track. *Acta Geologica Sinica*, 81(8): 1081–1098 (in Chinese with English abstract).

Eva, E., and John, I.G., 2016. Low-temperature thermochronology applied to ancient settings. *Journal of Geodynamics*, 93: 17–30.

Feng Shirong, 1998. Research of stable isotopes and its application to regional prognosis of sandstone-type uranium deposit of interlayer oxidation zone at northwest margin of Junggar Basin. *Uranium Geology*, 14(2): 102–106 (in Chinese with English abstract).

Fernandes, P., Cogne, N., Chew, D.M., Rodrifues, B., Jorge, R.C.G.S., Margues, J., Jamal, D., and Vasconcelos, L., 2015. The thermal history of the Karoo Moatize-Minjova Basin, Tete Province, Mozambique: an integrated vitrinite reflectance and apatite fission track thermochronology study. *Journal of African Earth Sciences*, 112(112): 55–72.

Franco Pirajno, Reimar Seltmann and Yang Yongqiang, 2011. A review of mineral systems and associated tectonic settings of northern Xinjiang, NW China. *Geoscience Frontiers*, 2(2): 157–185.

Fuchs, S., Schumann, D., Williams-Jones, A.E., and Vali, H., 2015. The growth and concentration of uranium and titanium minerals in hydrocarbons of the Carbon Leader Reef, Witwatersrand Supergroup. *South Africa Chemical Geology*, 393–394 : 55–66.

Guo Zhaojie, Chen Shi and Zhang Yuanyuan, 2017. The ophiolitic mélanges in strike-slip fault zones in west Junggar, Xinjiang, NW China. *Acta Geologica Sinica* (English Edition), 91(s1): 13–14.

He Dengfa, Yin Cheng, Du Shekuan, Shi Xi and Ma Huishu, 2004. Characteristics of structural segmentation of foreland thrust belts-a case study of the fault belts in the northwestern margin of Junggar Basin. *Earth Science Frontiers*, 11(3): 91–101 (in Chinese with English abstract).

He Dengfa, Zhou Lu, Tang Yong, Wu Xiaozhi and Du Shekuan, 2007. Characteristics of unconofrmity between the Xishanyao Formation and Toutunhe Formaiton of Middle Jurassic in Junggar Basin and its significance in petroleum exploration. *Journal of Palaeogeography*, 9(4): 387–396 (in Chinese with English abstract).

He Zhongbo, Qin Mingkuan, Huang Zhixin, Guo Qiang and Xu Qiang, 2014. Analysis on uranium mineralization prospect of Jurassic in northwest margin of Junggar Basin. *Xinjiang Geology*, 32(3): 400–404 (in Chinese with English abstract).

Hitzman, M.W., Selby, D., and Bull, S., 2010. Formation of sedimentary rock-hosted stratiform copper deposits through Earth history. *Economic Geology*, 105(3): 627–639.

Hu Yang and Xia Bin, 2012. An approach to the tectonic evolution and hydrocarbon accumulation in the Halaalate Mountain area, northern Xinjiang. *Sedimentary Geology and*

Tethyan Geology, 32(2): 52–58 (in Chinese with English abstract).

Huang Shaohua, Qin Mingkuan, Liu Zhangyue, Mao Lihua, He Zhongbo and Xu Qiang, 2016. Fluid inclusion and organic geochemistry characteristics of uranium-bearing sandstone in the Liuhuanggou area in the southern margin of Junggar Basin. *Acta Geological Sinica*, 90(3): 475–488 (in Chinese with English abstract).

Landais, P., 1996. Organic geochemistry of sedimentary uranium ore deposits. *Ore Geology Reviews*, 11(11): 33–51.

Li Li, Chen Zhengle, Qi Wanxiu, Wang Shixin, Chen Xuanhua, Wu Yiping, Gong Hongliang, Wei Xinchang, Yang Yi and Li Xuezhi, 2008. Apatite fission track evidence for uplifting-exhumation processes of mountains surrounding the Junggar Basin. *Acta Petrologica Sinaca*, 24(5): 1011–1020 (in Chinese with English abstract).

Li Wei, 2007. *The mechanic and tectonic evolution of Mesozoic basins in northwestern Junggar orogenic belt*. Beijing: Chinese Academy of Geological Sciences (Ph. D thesis): 10–89 (in Chinese with English abstract).

Li Zhenhua, 2011. *Analysis on the tectonic event and paleo-geothermal feature of Yanshanian in the northern Junggar Basin*. Xi'an: Northwest university (master dissertation): 7–59 (in Chinese).

Lin Shuangxing, 1997. Analysis of metallogenic conditions of sandstone type uranium deposits in interlayer oxidation zone in the northwest of Junggar Basin, Xinjiang. *Uranium Geology*, 13(2): 65–68 (in Chinese with English abstract).

Lin, X., Zheng, D.W., Sun, J.M., Windley, B.F., Tian, Z.H., Gong, Z.J., and Jia, Y.Y., 2015. Detrital apatite fission track evidence for provenance change in the Subei Basin and implications for the tectonic uplift of the Danghe Nan Shan (NW China) since the mid-Miocene. *Journal of Asian Earth Sciences*, 111: 302–311.

Liu, Z.Y., Peng, S.P., Qin, M.K., Liu, H.X., Geng, Y.Y., and Zhang, X., 2018. Origin and role of kaolinization in roll-front uranium deposits and its response to ore-forming fluids in the Yili basin, China. *Geofluids*, 2: 1–16.

Liu Zhangyue, Peng Suping, Qin Mingkuan, Liu Hongxu, Huang Shaohua and He Zhongbo, 2017. Multistage enrichment of the Sawafuqi uranium deposit: new insights into sandstone-hosted uranium deposits in the intramontane basins of Tianshan, China. *Acta Geologica Sinica* (English Edition), 91(6): 2138–2152.

Liu Zhangyue, Qin Mingkuan, Cai Gengqing, Liu Hongxu and Geng Yingying, 2015. The organic geochemical characteristics and its controls on uranium mineralization in the Bashibulake area, Xinjiang. *Earth Science Frontiers*, 22 (4): 212–222 (in Chinese with English abstract).

Liu Zhangyue, Qin Mingkuan, Liu Hongxu, Cai Gengqing, He Zhongbo, Guo Qiang, Xu Qiang and Song Jiye, 2016. Meso-Cenozoic orogeny in south Tianshan and resultant superimposed enrichment effect on the Sawabuqi uranium deposit. *Acta Geologica Sinica,* 90(12): 1–10 (in Chinese with English abstract).

Lu Kegai, 2005. Evaluation for the sandstone type uranium deposits in the Junggar Basin, Xinjiang. CNNC Geology Party No. 216, 12–202 (in Chinese).

Ma Delong, 2014. *The structural geometric and kinematic features of Wuerhe-Xiazijie thrust belt at the northwestern margin of Junggar Basin*. Beijing: China University of Geosciences (Master thesis): 11–74 (in Chinese).

Michel, C., 2010. Evolution of uranium fractionation processes through time: driving the secular variation of uranium deposit types. *Economic Geology*, 105(3): 553–569.

Muhammad, R.K., Fahad, H.M., Saleem, M., Muhammad, B., and Sohail, M., 2016. Tectonic study of the sub-Himalayas based on geophysical data in Azad Jammu and Kashmir and Northern Pakistan. *Journal of Earth Science*, 27(6): 981–988.

Qi, B.S., Hu, D.G., Yang, X.X., Zhang, Y.L., Tan, C.X., Zhang, P., and Feng, C.J., 2016. Apatite fission track evidence for the Cretaceous–Cenozoic cooling history of the Qilian Shan (NW China) and for stepwise northeastward growth of the northeastern Tibetan Plateau since early Eocene. *Journal of Asian Earth Sciences*, 124: 28–41.

Qiu Nansheng, Yang Haibo and Wang Xulong, 2002. Tectono-thermal evolution in the Junggar Basin. *Chinese Journal of Geology*, 37(4): 423–429 (in Chinese with English abstract).

Richard, L.R., and Martin, B.G., 1978. Origin of a South Texas roll-type uranium deposit: I. Alteration of iron-titanium oxide minerals. *Economic Geology*, 73(8): 1677–1689.

Roman, V.V., Stuart, N.T., Andrey, A.A., and Vladimir, S.Z., 2015. Apatite fission track thermochronology of Khibina Massif (Kola Peninsula, Russia): implications for post-Devonian tectonics of the NE Fennoscandia. *Tectonophysics*, 665: 157–163.

Shao Yu, Wang Renfu, Zhang Yueqian, Wang Xin, Li Zhenhua and Liang Han, 2011. Strike-slip structures and oil-gas exporation in the NW margin of Junggar Basin, China. *Acta Petrolei Sinica*, 32(6): 976–983 (in Chinese with English abstract).

Shen Yang, Lin Huixi, Zhao Leqiang, Zeng Zhiping, Gong Yajun, Guo Ruichao and Min Feiqiong, 2015. Hydrocarbon migration-accumulation characteristics and pool-forming patterns in overlap-erosion zones in northwestern margin of Junggar Basin. *Xinjiang Petroleum Geology*, 36(5): 505–509 (in Chinese with English abstract).

Silvia, K., Rastislav, V., Paul, A., Michal, K., Bernhard, F., Jozef, H., and Jozef, M., 2014. Late Cretaceous–Cenozoic thermal evolution of the northern part of the Central Western Carpathians (Slovakia): revealed by zircon and apatite fission track thermochronology. *Tectonophsics*, 615–616(4): 142–153.

Song Jiye, Qin Mingkuan, Cai Yuqi and He Zhongbo, 2015. Basement charateristics of Junggar Basin and its effect on sandstone-type uranium metallogenesis. *Geological Review*, 61(1): 128–137 (in Chinese with English abstract).

Stijn Glorie, and Johan De Grave, 2016. Exhuming the Meso-Cenozoic Kyrgyz Tianshan and Siberian Altai-Sayan: A review based on low-temperature thermochronology. *Geoscience Frontiers*, 7(2): 155–170.

Sui Fenggui, 2015. Tectonic evolution and its relationship with hydrocarbon accumulation in the northwest margin of Junggar Basin. *Acta Geologica Sinica*, 89(4): 779–793 (in Chinese with English abstract).

Tan Kaijun, Zhang Fan, Zhao Yingcheng, Tan Jiqiang, Guan Yinlu and Yang Zhidong, 2008. Comparative analysis on the segmentation of tectonic characteristic in northwest Junggar Basin. *Petroleum Geology and Engineering*, 22(2): 1–3 (in Chinese with English abstract).

Wang Huimin, Wu Hua, Jin Tao and Yang Hongxia, 2005. Rule of hydrocarbons accumulation in the northwest edge of

Junggar Basin. *Xinjiang Geology*, 23(3): 279–282 (in Chinese with English abstract).

Wang Renfu, 2011. *Stuctural analysis of Kalamay-Xiazijie strike -slip fault zone in NW margin of Junggar Basin, Xinjiang, China*. Hangzhou: Zhejiang University (Ph. D thesis): 21–98 (in Chinese).

Wu Yuanyan, Ping Junbiao, Lv Xiuxiang, Xu Youde and Fu Jianlin, 2002. Quantitative research on preservation and destruction of hydrocarbon accumulation in the northwest edge of Junggar Basin. *Acta Petrologica Sinica*, 23(6): 24–28 (in Chinese with English abstract).

Wu, L.Q., Jiao, Y.Q., Roger, M., and Yang, S.K., 2009. Sedimentological setting of sandstone-type uranium deposits in coal measures on the southwest margin of the Turpan-Hami Basin, China. *Journal of Asian Earth Sciences*, 36(2): 223–237.

Xu Jiandong, Ma Zhongjin, Qu Guosheng and Li Jun, 2008. Study on basin-range coupling along northwestern margin of Junggar Basin. *Xinjiang Petroleum Geology*, 29(2): 143–146 (in Chinese with English abstract).

Yang Yongqiang, Qiu Longwei, Cao Yingchang, Chen Cheng, Lei Dewen and Wan Ming, 2017. Reservoir quality and diagenesis of the Permian Lucaogou Formation tight carbonates in Jimsar sag, Junggar Basin, West China. *Journal of Earth Science*, 28(6): 1032–1046.

Yang, X.Y., Ling. M.X., Sun, W.D., Luo, X.D., Miao, J.Y., and Sun, W., 2014. The genesis of sandstone-type uranium deposits in the Ordos Basin, NW China: constraints provided by fluid inclusions and stable isotopes. *International Geology Review*, 51(5): 422–455 http://dx.doi.org/10.1080/00206810902757339.

Yuan Wanming, Du Yangsong, Yang Liqiang, Li Shengrong and Dong Jinquan, 2007. Apatite fission track studies on the tectonics in Nanmulin area of Gangdese terrane, Tibet plateau. *Acta Petrologica Sinica*, 23(11): 2911–2917 (in Chinese with English abstract).

Zhang Beihang, Zhang Jin, Wang, Yannan, Zhao Heng and Li Yanfeng, 2017. Late Mesozoic–Cenozoic exhumation of northern Hexi Corridor: constrained by apatite fission track age of the Longshoushan. *Acta Geologica Sinica* (English Edition), 91(5): 1624–1643.

Zhang Quanqing, Zhang Xinke and Ren Manchuan, 2009. Analysis on hydrological condition for uranium ore formation in Wuerhe district, Junggar Basin. *World Nuclear Geoscience*, 26(2): 76–80 (in Chinese with English abstract).

Zhang Shanwen, 2013. Hydrocarbon accumulation characteristics and exploration prospects of stratigraphic unconformity in basin margin of Junggar Basin. *Petroleum Geology & Experiment*, 35(3): 231–248 (in Chinese with English abstract).

Zhao Bai,1992. Formation and evolution of Junggar Basin. *Xinjiang Petroleum Geology*, 3(1): 192–195 (in Chinese with English abstract).

About the first author

QIN Mingkuan, male; born in 1968 in Sichuan Province, Doctor, uranium geology, Professor of Beijing Research Institute of Uranium Geology, CNNC. His current research mainly focuses on sandstone-hosted uranium deposit. E-mail: qinmk9818@163.com.